11th AIAA/CEAS Aeroacoustics Conference (26th AIAA Aeroacoustics Conference)
23 - 25 May 2005, Monterey, California

AIAA 2005-2956

DNS of a High-Aspect-Ratio Elliptic Vortex and its Generated Noise

Sébastien Barré,* Christophe Bogey† and Christophe Bailly‡
Laboratoire de Mécanique des Fluides et d'Acoustique
École Centrale de Lyon & UMR CNRS 5509
69134 Ecully, France.

The aerodynamic evolution and the acoustic radiation of elliptic vortices with various aspect ratios are investigated by solving numerically the full compressible Navier–Stokes equations. Three behaviours are observed according to the aspect ratio $\sigma = a/b$ where a and b are the major and minor semi-axes of the vortices. At the small aspect ratio $\sigma = 1.2$, the vortex rotates at a constant angular velocity and radiates like a rotating quadrupole. The acoustic radiation is in very good agreement with a reference analytical solution. At the moderate aspect ratio $\sigma = 5$, the vortex is initially unstable. However, its aspect ratio decreases due to an axisymmetrization process, which inhibites the growth of instabilities. The noise level then decreases and the radiation frequency increases. The far-fied is found to be in good agreement with the reference solution, which has been modified to take into account the evolution of the shape of the vortex. For vortices with larger aspect ratios $\sigma \geq 6$, axisymmetrization does not occur quickly enough to stop the growth of instabilities, which splits the vortices. Then various mergings are found to occur. For instance in the case $\sigma = 6$, several successive switches between an elliptic state and a configuration of two co-rotating vortices are observed. The sound field remains weakly affected by the switches. The present results show that the initial value of the aspect ratio yields the relative weight of the axisymmetrization which stabilizes the vortex, and of the growth of instabilities which tends to split it.

I. Introduction

Two-dimensional flows such as simple vortices have been intensively investigated in the past. These configurations seem elementary, but they are very useful to understand the evolution of coherent structures in numerous flows. For instance, elliptic vortices allow to consider vortical configurations encountered in geophysical flows (Miyazaki & H. Hanazaki[1] and Miyazaki *et al.*[2]) or to model anisotropic effects of vortices (Dritschel & Legras[3] and Legras & Dritschel[4]).

The first works on elliptic vorticity distributions were analytical investigations of Kirchhoff's vortex (1876), see Lamb[5] and Love.[6] This top hat vortex rotates at a constant angular velocity Ω_{th} without change of shape. Love[6] demonstrated that it is linearly stable for aspect ratios $\sigma = a/b < 3$, a and b being the major and minor semi-axes of the ellipse. Dritschel[7] also shown numerically that the vortex is nonlinearly stable only in the range of the linear stability $\sigma < 3$. Note also that the stability of the vortex has recently been linked by Vosbeek *et al.*[8] to the spatial distribution of the strain rate, which must be of lower amplitude inside the vortex than just outside to ensure the stability. If $\sigma > 3$ the vortex is unstable, and the growth

*PhD Student, sebastien.barre@ec-lyon.fr
†CNRS Reasearch Scientist, christophe.bogey@ec-lyon.fr
‡Professor, Senior Member AIAA, christophe.bailly@ec-lyon.fr

of instabilities can dramatically alter the shape of the vortex and can split it into two or more co-rotating vortices. The conditions for which the split generates two vortices have been investigated from energetic considerations by Dritschel.[7,9] In particular, this case is preferentially observed for an aspect ratio close to six. The time evolution of the vortex can be also affected by the process of axisymmetrization. Melander *et al.*[10] have indeed shown that, for a vortex with smooth boundaries, some vorticity is progressively shedded through the formation of filaments, leading to a circular vortex. This phenomenon has been studied for stable elliptical vortices and has also been observed for co-rotating vortices by Melander *et al.*[11] However the circular state appears not to be obtained for vortices with sufficiently steep edge gradients as reported by Dritschel.[12]

Thus, two phenomena, namely the growth of instabilities and the axisymmetrization, occur in the case of an unstable Kirchhoff vortex. Instabilities may grow, and tend to split the vortex. In the same time, the axisymmetrization process takes place and can affect the growth of these instabilities. Therefore, the evolution of the vortex depends on the process which will dominate the other one. The dominant process is usually determined during the first few revolutions. The vortex development during this step can indeed change the relative weight of the two processes. In particular, as pointed out by Melander *et al.*[10] viscosity may play an important role during the initial evolution of vortices with sharp gradients of vorticity. A careful calculation of the viscous effects is therefore required to study numerically the Kirchhoff vortex properly. Unfortunately most of the computational studies in the literature are based on pseudospectral methods (see Melander *et al.*[10]) or on the contour dynamic method (see Dritschel[7,12] and Vosbeek *et al.*[8]). Since viscosity is provided by an artificial fourth-order viscosity in pseudospectral algorithms, and is even neglected in the contour dynamic methods, only inviscid or weakly dissipative flows can be studied with such approaches. Thus, these methods fail in computing the behaviour of Kirchhoff's vortices accurately when the competition between the growth of instabilities and the axisymmetrization occurs. Moreover the numerical methods mentionned above are restricted to incompressible flows, implying that the noise radiated by elliptic vortices could not be directly calculated in these previous works.

In the present paper, the behaviours of Kirchhoff's vortices with initial aspect ratios $\sigma = 1.2$, 5, 6 and 25 are calculated, using accurate numerical techniques developed recently by Bogey & Bailly[13] for the direct computation of aerodynamic noise (see Bogey *et al.*,[14] Bogey & Bailly[15] and Gloerfelt *et al.*[16]). The full compressible Navier–Stokes equations are solved to obtain the flow field and the acoustic radiation in the same calculation. The noise generated by two circular co-rotating vortices has already been investigated by Colonius *et al.*[17] and Bogey *et al.*[18] thanks to this approach. In the first case $\sigma = 1.2$, the elliptic vortex is stable and very similar to a circular vortex. For $\sigma = 5$, the axisymmetrization is expected to occur. For $\sigma \geq 6$ the vortex is strongly unstable and the growth of instabilities may have a notable effect on the vortex evolution. The objectives are to study the effects of the competition between the axisymmetrization process and the nonlinear evolution of instabilities on the time evolution of the vortex and to find the range of σ in which each phenomenon dominates the other one. Moreover, the noise generated by vortices with aspect ratios $1.2 \leq \sigma \leq 6$ is investigated with the aim of showing the influence of the initial aspect ratio on the acoustic radiation and the effects of the axisymmetrization on the pressure field.

In the present paper, §II describes the numerical algorithm and the initial conditions used. The case of an aspect ratio close to unit, $\sigma = 1.2$, is investigated in §III and the case of the moderate aspect ratio $\sigma = 5$ is studied in §IV. The acoustic results are connected to the aerodynamic field and are also compared to the reference solution obtained by Howe[19] and presented in the appendix. Finally, §V is devoted to two configurations with large aspect ratios $\sigma = 6$ and 25. In particular, the radiated noise in the case $\sigma = 6$ is calculated and the switch between an elliptic vortex and a configuration of two vortices is shown.

II. Numerical method

A. Governing equations

The two-dimensional compressible Navier–Stokes equations are solved in the conservative form

$$\frac{\partial \boldsymbol{U}}{\partial t} + \frac{\partial \boldsymbol{E}_e}{\partial x_1} + \frac{\partial \boldsymbol{F}_e}{\partial x_2} - \frac{\partial \boldsymbol{E}_v}{\partial x_1} - \frac{\partial \boldsymbol{F}_v}{\partial x_2} = 0$$

where $\boldsymbol{U} = (\rho, \rho u_1, \rho u_2, \rho e_t)^{\mathrm{t}}$ is the unknown vector. The variables ρ, u_1, u_2 and e_t are respectively the density, the two velocity components and the total specific energy. The subscripts e and v denote the Euler and the viscous fluxes. For a perfect gas

$$\rho e_t = \frac{p}{\gamma - 1} + \frac{1}{2}\rho \left(u_1^2 + u_2^2\right)$$

where γ is the specific heat ratio and p the pressure. The Euler fluxes are given by

$$\boldsymbol{E}_e = \begin{pmatrix} \rho u_1 \\ \rho u_1^2 + p \\ \rho u_1 u_2 \\ (\rho e_t + p) u_1 \end{pmatrix} \qquad \boldsymbol{F}_e = \begin{pmatrix} \rho u_2 \\ \rho u_1 u_2 \\ \rho u_2^2 + p \\ (\rho e_t + p) u_2 \end{pmatrix}$$

and viscous fluxes by $\boldsymbol{E}_v = (0, \mathcal{T}_{11}, \mathcal{T}_{12}, u_i \mathcal{T}_{1i})^{\mathrm{t}}$ and $\boldsymbol{F}_v = (0, \mathcal{T}_{21}, \mathcal{T}_{22}, u_i \mathcal{T}_{2i})^{\mathrm{t}}$. The viscous stress tensor is defined by $\mathcal{T}_{ij} = 2\mu \mathcal{S}_{ij}$ where μ is the dynamic molecular viscosity and $\mathcal{S}_{ij}$ the deviatoric part of the deformation stress tensor

$$\mathcal{S}_{ij} = \frac{1}{2}\left(\frac{\partial u_i}{\partial x_j} + \frac{\partial u_j}{\partial x_i} - \frac{2}{3}\delta_{ij}\frac{\partial u_k}{\partial x_k}\right)$$

B. Numerical algorithm

Numerical schemes with low-dispersion and low-dissipation properties developed by Bogey & Bailly[13] are used. The spatial discretization is performed by an eleven-point stencil finite-difference scheme optimized in the wave-number space ensuring accuracy up to four points per wavelength. An optimized explicit six-stage Runge-Kutta algorithm is applied for time integration. To ensure stability, grid-to-grid oscillations are removed thanks to an eleven-point stencil selective filter without affecting the resolved scales, since only the short waves discretized by less than four points per wavelength are damped. Note that in the present work, Direct Numerical Simulations of the Navier–Stokes equations are performed, without turbulence modelling. Moreover, the two-dimensional non-reflecting boundary conditions proposed by Tam & Webb[20] are implemented. They are derived from the asymptotic solution of Euler's equations in the acoustic far-field, and thus allow to minimize acoustic reflections. This point is crucial for the direct calculation of the acoustic field.

C. Numerical specifications and initial conditions

The mesh used is a Cartesian grid with 381×381 points. The discretizations in the x_1 and x_2 directions are the same and are symmetrical with respect to the center of the grid. The mesh spacing is uniform for the first thirty points close to the center with a mesh spacing of $\Delta_0 = 2 \times 10^{-4}$m. Then a streching rate of 4% is applied to the 95 next grid points to include a large part of the radiated acoustic field in the computational domain. This streching rate is small enough to keep the high accuracy of the numerical schemes (see Bogey & Bailly[13]). The largest mesh spacing is thus $\Delta_{max} = 41.5\ \Delta_0$. Finally, the mesh spacing remains uniform

for the final 65 points. This mesh grid is sufficiently fine to enable an accurate propagation of the waves in the cases studied in this paper. A case has for instance been investigated with a mesh spacing twice smaller and has demonstrated that the use of a finer grid does not modify the results. The origin of the axes is taken at the center of the grid. The computational domain extends from $-3.7 \times 10^3 \Delta_0$ up to $3.7 \times 10^3 \Delta_0$ in both Cartesian directions. All the simulations are made with $CFL = c_\infty \Delta t / \Delta_0 = 1$, where c_∞ is the sound speed in the ambient medium and Δt is the time step.

The calculations are initialized by the Kirchhoff elliptic vortex, an elliptic patch of uniform vorticity, which is an exact analytical solution of the two-dimensional Euler equations (see Lamb[5]). Pressure and density are respectively initialized by the ambiant pressure and density, p_∞ and ρ_∞. The variable ω is the vorticity inside the vortex and the quantity ϵ, called ellipse parameter, is defined by the relation $\sigma = (1+\epsilon)/(1-\epsilon)$. The radius r_e of the circle associated with the ellipse is then connected to the semi-axes by $a = r_e(1+\epsilon)$ and $b = r_e(1-\epsilon)$. The subscript 0 denotes a quantity taken at $t = 0$. For example, a_0 is the initial major semi-axis. The initial angular velocity of the vortex is Ω_0 and T_0 corresponds to the initial period of rotation. In all simulations, r_{e0} is set to $40\,\Delta_0$. This ensures an appropriate discretization of the geometry and of the dynamics of the vortex for $\sigma \leq 25$. The initial vorticity is $\omega_0 = 0.027/\Delta t$, providing an accurate time discretization. The Reynolds numbers based on the major semi-axis a_0 and on the maximum of the velocity on the edge of the vortex are 1.1×10^5 for $\sigma = 1.2$ down to 2.8×10^4 for $\sigma = 25$. The values taken by a and b are computed at each time step. They are evaluated from the contour of the vorticity with a threshold chosen arbitrarily as $\omega_{max}/2$, where ω_{max} is the maximum of vorticity in the vortex. The other parameters of the ellipse are then deduced.

III. Vortex with an aspect ratio close to unit ($\sigma_0 = 1.2$)

The case of an elliptic vortex with a small aspect ratio is first investigated. The initial aspect ratio is $\sigma_0 = 1.2$, which yields for the ellipse parameter $\epsilon_0 = 0.09 \ll 1$. First, the aerodynamic behaviour is discussed and compared to the theoretical results developed for the Kirchhoff elliptic vortex. Then the acoustic radiation is shown and compared to the analytical solution (3). In this case, the analytical formulation reported in the appendix is expected to be valid.

A. Aerodynamic results

Figure 1(a) shows isolevels of vorticity at time $t/T_0 = 16$. No filamentation process is observed, even after 16 revolution periods. To understand this, the streamlines of the initial vortex in a rotating frame associated to its theoretical angular velocity $\Omega_{th} = \omega(1-\epsilon^2)/4$ (see Lamb[5]) are displayed in figure 1(b). The streamline pattern keeps the same structure during the whole evolution time. Melander *et al.*[10] pointed out that the axisymmetrization can occur only when the two saddle points A and B are located in the vorticity core. In that case, the vorticity around these points is carried away from the core and follows the streamlines, beginning the filamentation process. For a perfect top-hat vortex, the saddle points A and B are outside the patch of vorticity, as shown in figure 1(b), and thus the shedding cannot occur. In the present computation, the viscous diffusion at the vortex edge tends to relaxe the gradients. However, the vortex does not become smooth enough to include the saddle points and the filamentation cannot begin. As previously observed by Dritschel,[12] vortices with sufficiently steep edge gradient do not seem to axisymmetrize. This point is also supported by the time evolution of the aspect ratio σ in figure 2(a). The aspect ratio remains practically constant for $t < 15T_0$, indicating that the vortex rotates without significant change of form.

In figure 2(b), the time history of the computed angular velocity Ω/Ω_0 is shown to be constant and in good agreement with the theoretical value $\Omega_{th}/\Omega_0 = \omega(1-\epsilon^2)/(4/\Omega_0)$ given by Love[6] for Kirchhoff's vortex. This theoretical velocity is calculated at each time step from the values of ϵ and ω, where ω is estimated by the mean integral level of vorticity inside the contour level $\omega_{max}/2$. During the rotation, the vortex edge becomes smoother due to viscous diffusion and the area of the vortex increases slightly. This implies a low decrease of the mean integral level of vorticity and thus the small reduction of Ω_{th} observed in figure 2(b).

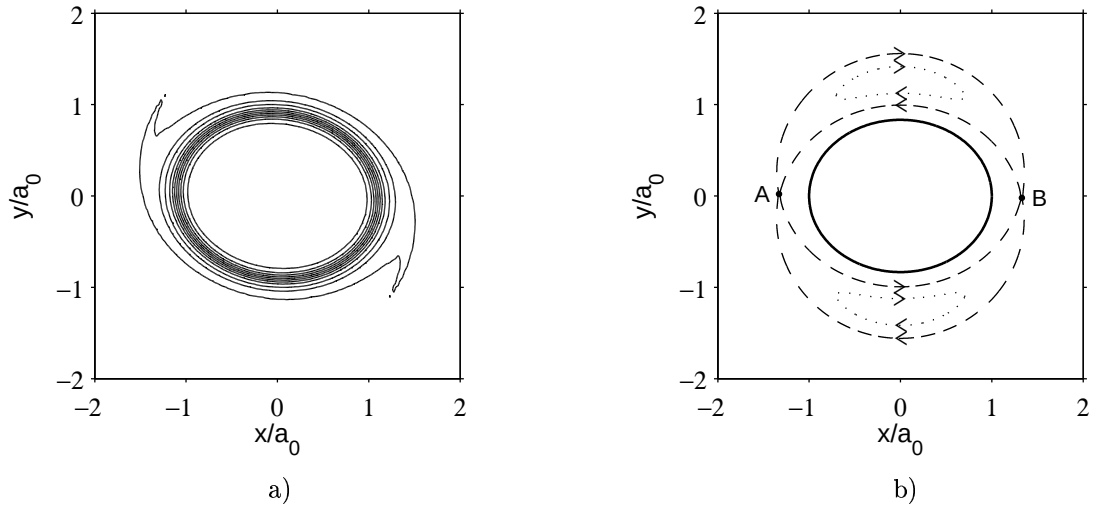

Figure 1. Case $\sigma_0 = 1.2$. a) Isolevels of vorticity at time $t/T_0 = 16$. Levels: 1%, 5%, and from 10% to 90% of the maximum of vorticity with a 10% step. b) Streamlines of the initial Kirchhoff vortex in a frame rotating with the angular velocity $\Omega_{th} = \omega(1 - \epsilon^2)/4$. ——— edge of the vortex; ----- and ···· streamlines. The points A and B are the two saddle points.

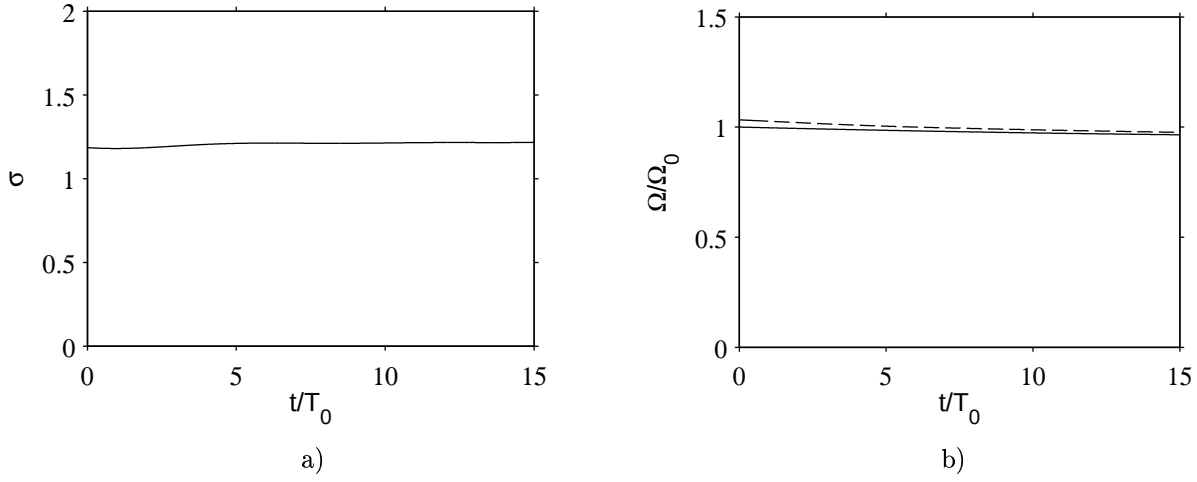

Figure 2. Case $\sigma_0 = 1.2$. a) Time history of σ. b) ——— Time evolution of the computed angular velocity Ω/Ω_0; ----- theoretical velocity Ω_{th}/Ω_0.

B. Acoustic radiation

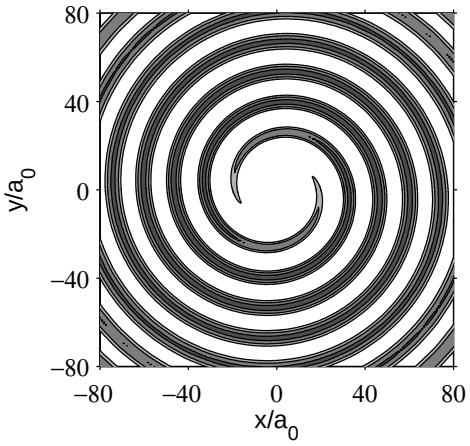

Figure 3. Case $\sigma_0 = 1.2$. Pressure field at time $t/T_0 = 16$. Contour levels: $p_\infty - 10$ Pa, p_∞ and $p_\infty + 10$ Pa.

The acoustic radiation of the vortex is now investigated. The elliptic vortex radiates like a rotating quadrupole as shown with the pressure field in figure 3. The pressure along the line $x = y$, $x > 0$, at time $t = 16T_0$, is displayed in figure 4(a). The magnitude of the acoustic near-field is shown to decrease rapidly when the observation point moves away from the vortex. In this figure, the computed acoustic field is compared to the analytical formulation (3) reported in the appendix. This formulation has been obtained by Howe[19] and provides the acoustic far-field generated by the vortex. It is appropriate for Kirchhoff's vortices with $\epsilon \ll 1$, for which viscous effects are neglected. By considering only the first order in ϵ, Howe has thus obtained that the noise level is proportional to ϵ and that the pulsation of the radiated noise does not depend on the aspect ratio. Note that an extended formulation (4), taking into account the effective motion of the vortex for the radiation frequency, is also detailed in the appendix. This extended formulation can be applied in cases where the elliptical shape of the vortex evolves with time, using parameters updated at the corresponding retarded times. Moreover, the analytical solutions (3) and (4) do not provide the near-field contribution. In the present case, for $d/a_0 \geq 80$, the far acoustic field dominates the pressure field and the computational result tends to the analytical formulation, with a good agreement in frequency and level. In the graph 4(b), the comparison for an observation point in the far-field at $d/a_0 \simeq 80$ illustrates this good agreement.

IV. Vortex with a moderate aspect ratio ($\sigma_0 = 5$)

In this section, an elliptic vortex with a moderate aspect ratio of $\sigma_0 = 5$ is investigated. This aspect ratio corresponds to the parameter $\epsilon_0 = 0.67$. The dynamics of the vortex should now be significantly affected by the growth of instabilities and by the axisymmetrization process. Moreover the analytical solution (3) might not be appropriate for describing the acoustic far-field.

A. Stability of Kirchhoff's vortex

The linear stability of the Kirchhoff vortex was first studied by Love.[6] By noting δn the normal displacement of the edge of the vortex, the eigenfunction of the small perturbation in a linear analysis writes as $\delta n \sim \exp\left[\mathrm{i}(m(\theta - \beta) - \gamma t)\right]$ where m is the azimuthal wavenumber, θ is the polar angle, β is a phase coefficient and $\gamma = \gamma_r + \mathrm{i}\gamma_i$ is the complex angular frequency. Thus γ_i corresponds to the growth rate of the

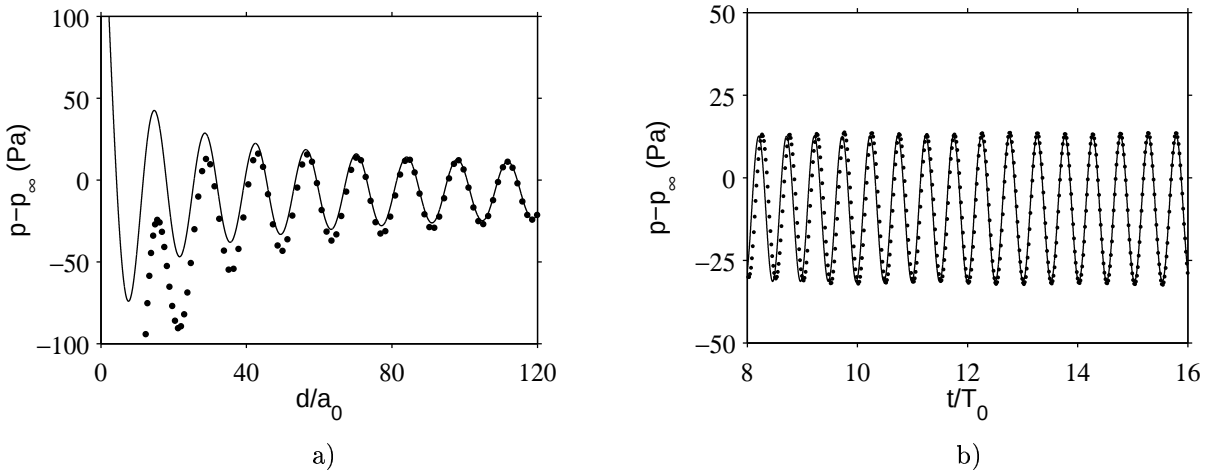

Figure 4. Case $\sigma_0 = 1.2$. Comparison of the acoustic radiation with the analytical solution (3): —— analytical solution; • computation. d is the distance from the vortex center. a) Pressure along the line $x = y$, $x > 0$ at time $t = 16T_0$. b) Time evolution of the pressure at the point $x/a_0 = y/a_0 = 56$.

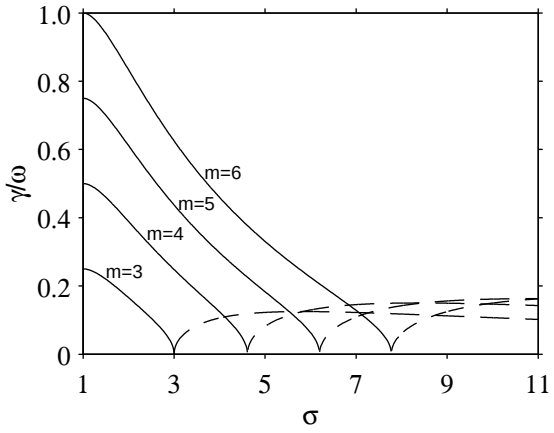

Figure 5. Linear stability of the modes $m = 3$, 4, 5 and 6 of the Kirchhoff vortex. $\gamma = \gamma_r + \mathrm{i}\gamma_i$ is the complex angular frequency of a mode and m is the azimuthal wavenumber. —— frequency γ_r; - - - - growth rate γ_i.

instabilities. The dispersion relation is given by $4\gamma^2/\omega^2 = (2m\lambda_1 - 1)^2 - \lambda_2^2$ where $\lambda_1 = \sigma/(1+\sigma)^2$ and $\lambda_2 = (\sigma-1)^m/(\sigma+1)^m$, see Dritschel.[7]

The stability of the azimuthal modes $m = 3$, 4, 5 and 6 is illustrated in figure 5. The modes $m = 1$ and $m = 2$ are not of interest since the mode $m = 1$ is always stable and the mode $m = 2$ is neutral with $\gamma_{m=2} = 0$ for all σ. For $m \geq 3$, γ is real for small σ, which imply linear stability. Above a critical value σ_{mc}, γ becomes imaginar and the mode m is then linearly unstable. For the mode $m = 3$, $\sigma_{3c} = 3$ is found and, for $m > 3$, $\sigma_{mc} > \sigma_{3c}$. For $\sigma < 3$, the vortex is therefore linearly stable and above this value there is always at least one mode linearly unstable.

The nonlinear stability was numerically investigated by Dritschel.[7] For $\sigma < 3$, the vortex is nonlinearly stable since it is linearly stable. For $3 < \sigma < 4.61$, *i.e.* when only the mode $m = 3$ is linearly unstable, only the odd perturbations are nonlinearly unstable. In a case where the initial disturbances are only even, there will be not growing instabilities. Dritschel shows indeed that even perturbations can only generate even modes through nonlinear effects and in the considered range of σ, all the even modes are stable. Finally, for $\sigma > 4.61$, at least one odd and one even mode are linearly unstable, $m = 3$ and $m = 4$ for example. Thus the vortex is nonlinearly unstable because the nonlinear effects will generate from any disturbance at least either the mode $m = 3$ or the mode $m = 4$, which are both unstable.

B. Aerodynamic results

The vorticity field is plotted in figure 6. For this case with $\sigma_0 = 5$, the filamentation process begins after about one revolution. The aspect ratio then decreases, as observed in snapshots of figures 6(c) and 6(d). Figure 7 shows the computed streamlines leaded by the vortices in the cases $\sigma_0 = 1.2$ and $\sigma_0 = 5$. As discussed in the previous section, the saddle points are initially far from the vortex in the case $\sigma_0 = 1.2$. When σ_0 is higher, the saddle points are initially closer to the boundary of the vortex, as in the present case $\sigma_0 = 5$ in figure 7(b), and some vorticity can reach them. Thus the filamentation process can take place.

The time history of the aspect ratio is shown in figure 8(a). Two steps in the evolution of the vortex are visible. The first step occurs from $t = 0$ to about $t = 2T_0$. Since $\sigma_0 > \sigma_{4c}$, the vortex is initially nonlinearly unstable and the initial perturbations are growing, as observed in figure 6(a) where the vortex is no more elliptic. In the same time the shedding of vorticity begins. The vorticity field in figure 6(a) shows the first step of this process and the filamentation clearly occurs in figure 6(b). As a result, the aspect ratio decreases down to the threshold σ_{4c}. Below this value, only odd perturbations are unstable. In the present simulations, the initial aerodynamic field is even and developing perturbations are consequently even, thus the vortex becomes stable for $\sigma < \sigma_{4c}$. This first step illustrates the opposite effects of the axisymmetrization and of the instabilities. The shedding of vorticity stabilizes the vortex whereas the growth of instabilities tends to split it. In the present case, the growth of instabilities is slow with respect to the period of rotation, therefore the axisymmetrization is the dominant phenomenon.

From about $t = 2T_0$, the second step is observed. The vortex remains elliptic and sheds vorticity. The aspect ratio decreases and this affects the angular velocity, which increases as reported in figure 8(b). This demonstrates that the time variations of the aspect ratio now strongly modify the behaviour of the vortex. A good agreement is found between the computed velocity Ω and the theoretical velocity $\Omega_{th} = \omega(1-\epsilon^2)/4$, given by Lamb[5] for the Kirchhoff vortex. Moreover, a significant discrepancy is observed between the theoretical velocity and the approximated velocity $\omega/4$, used by Howe[19] in the analytical formulation (3), showing that ϵ cannot be neglected if the aspect ratio is not close to unit.

The variations of the vorticity ω are directly connected to the evolution of the approximated velocity $\omega/4$, displayed in figure 8(b). The level of vorticity inside the vortex is thus shown to decrease with time. This occurs not only because of the slight viscous dissipation but also mainly because of the shedding of vorticity. Due to the expression of the theoretical velocity of the Kirchhoff vortex $\Omega_{th} = \omega(1-\epsilon^2)/4$, the decrease of ω implies a lowering of the angular velocity of the vortex. Thus, the filamentation tends to reduce the angular velocity throught the decrease of ω. The other effect of the axisymmetrization is the decrease of the aspect ratio and consequently of the parameter ϵ. The expression of the theoretical velocity Ω_{th} shows that this

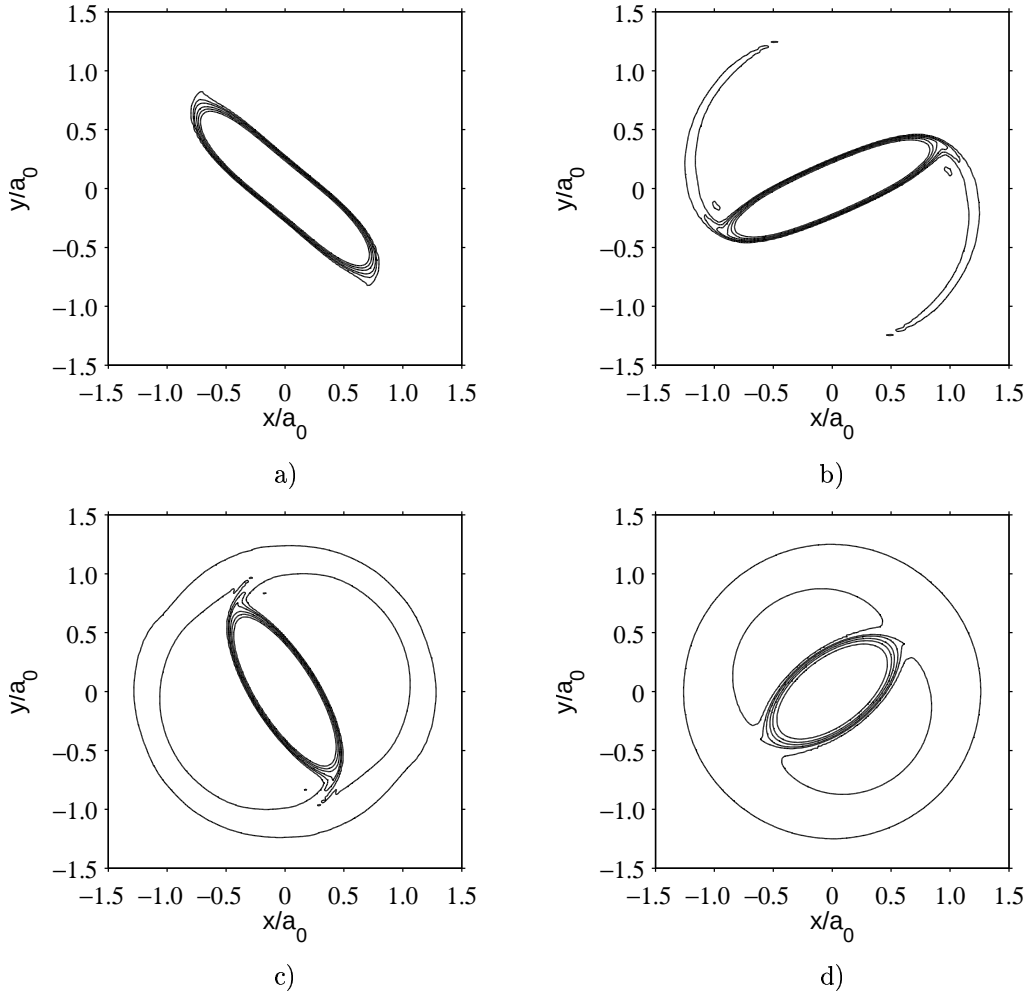

Figure 6. Case $\sigma_0 = 5$. Isolevels of vorticity at successive times: a) $t/T_0 = 0.91$; b) $t/T_0 = 1.6$; c) $t/T_0 = 4.0$; d) $t/T_0 = 11$. Levels: 2%, 10%, from 20% to 80% of the maximum of vorticity with a 20% step.

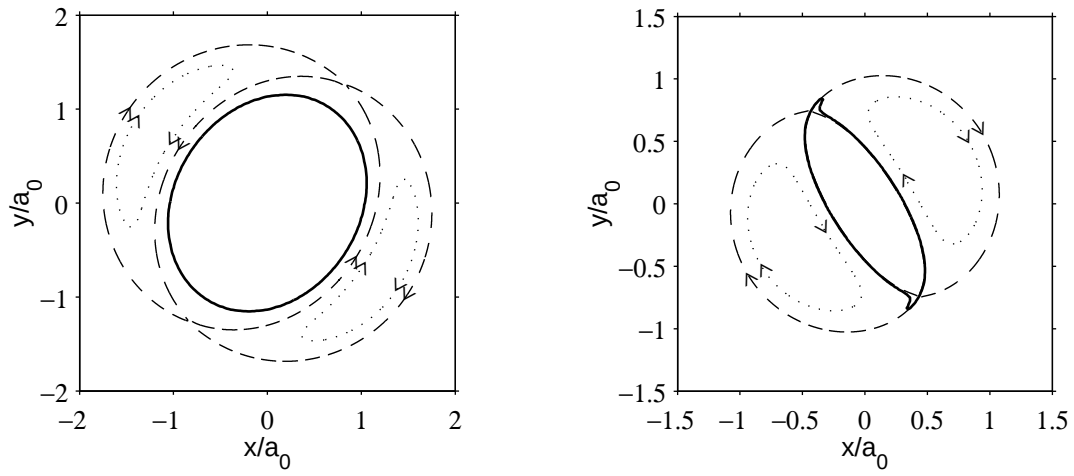

Figure 7. Computed streamlines of the vortex in a frame rotating with the angular velocity of the vorticity patch; ——— contour level of vorticity $0.1 \times \omega_{max}$; - - - - - and · · · · streamlines. a) Case $\sigma_0 = 1.2$ at time $t/T_0 = 12.6$. b) Case $\sigma_0 = 5$ at time $t/T_0 = 4.0$.

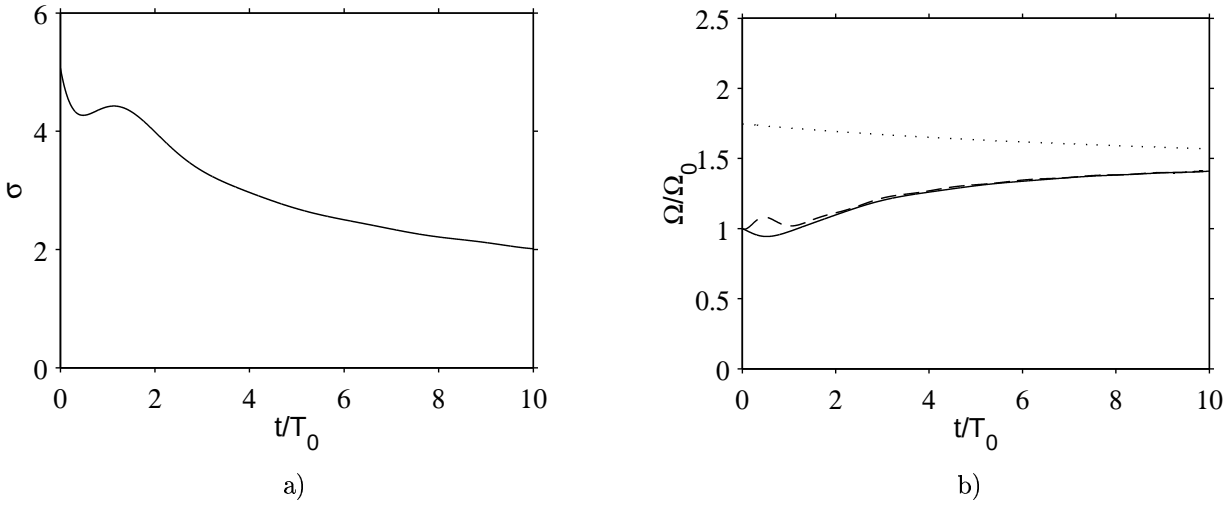

Figure 8. Case $\sigma_0 = 5$. a) Time evolution of σ. b) Time history of the dimensionless angular velocity; ——— effective velocity Ω/Ω_0; - - - - - theoretical velocity $\Omega_{th}/\Omega_0 = \omega(1-\epsilon^2)/(4\Omega_0)$; · · · · approximated velocity $\omega/(4\Omega_0)$.

process implies an acceleration of the rotation. Therefore, the shedding of vorticity has two opposed effects. According to the increase of the effective velocity Ω observed in the figure 8(b), the second effect is clearly dominant and the variations of the angular velocity are mainly due to the decrease of the aspect ratio, and not to the lowering of the vorticity level in the vortex core.

C. Acoustic radiation

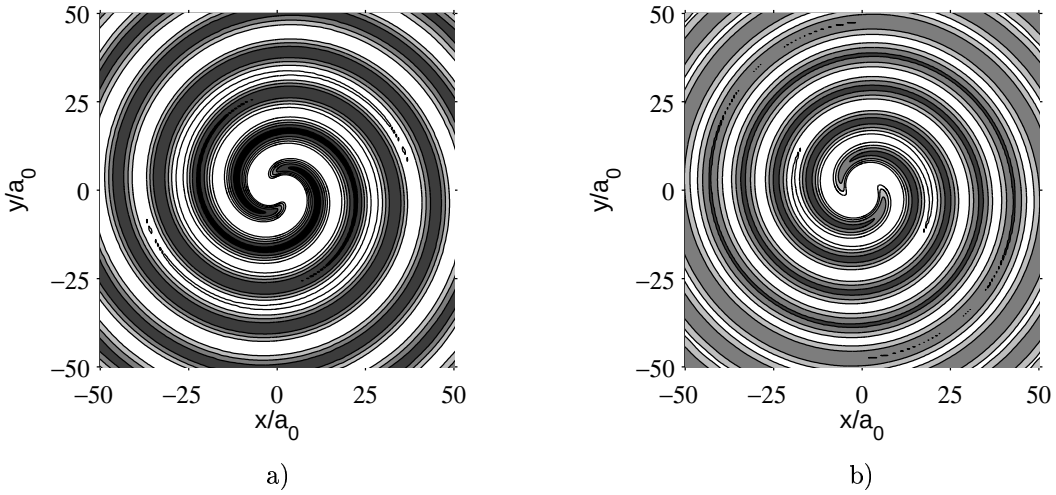

Figure 9. Case $\sigma_0 = 5$. Pressure field at time $t/T_0 = 4.0$ (a) and time $t/T_0 = 11$ (b). Contour levels: $p_\infty - 40$ Pa, $p_\infty - 20$ Pa, p_∞, $p_\infty + 20$ Pa and $p_\infty + 40$ Pa.

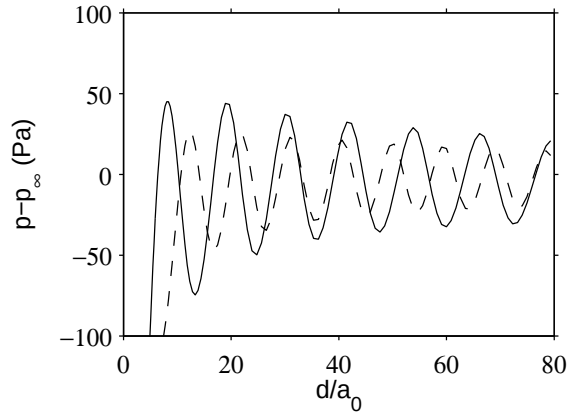

Figure 10. Case $\sigma_0 = 5$. Pressure profiles along the line $x = y$, $x > 0$ at two different times: —— $t = 4T_0$; - - - - - $t = 11T_0$ (d is the distance from the vortex center).

Snapshots of the pressure field at times $t = 4T_0$ and $t = 11T_0$, and the corresponding profiles along the line $x = y$, $x > 0$, are presented in figures 9 and 10. The axisymmetrization process is found to affect the sound field radiated by the vortex significantly. The radiation frequency increases with time, as expected due

to the increase of the angular velocity. Furthermore the noise level decreases, as predicted by the analytical expression (4).

In what follows, the computed pressure field is compared to the solution provided by expression (4) and not to the solution given by expression (3). Expression (4) takes into account the effective motion of the vortex and, in particular, the changes of the angular velocity in the modelling of the noise frequency, whereas in expression (3) the angular velocity is assumed to be constant. In the present case, the evolution of the radiation frequency is not negligible as shown in figure 10, and has indeed to be considered to provide an accurate description of the sound field.

The computed pressure profile along the line $x = y$, $x > 0$ at $t = 11T_0$ is plotted in figure 11(a) with the profile given by expression (4). Near the vortex, the comparison is not relevant since expression (4) does not provide the near pressure field. Farther from the vortex, a good agreement is observed between the numerical and the analytical solutions. The time history of the pressure at the location $x/a_0 = y/a_0 = 37$ is also displayed in figure 11(b). The computed and analytical results are found to be very close. This shows that the radiation frequency is accurately predicted by expression (4) taking into account the effective rotation of the vortex. Moreover, since in expression (4) only the first order in ϵ is kept for the amplitude, this good agreement also indicates that the level of the radiated noise is proportionnal to ϵ. This is remarkable in the present case where the parameter $\epsilon_0 = 0.67$ is not negligible. The present results thus demonstrate that expression (4) is appropriate over a large range of aspect ratios.

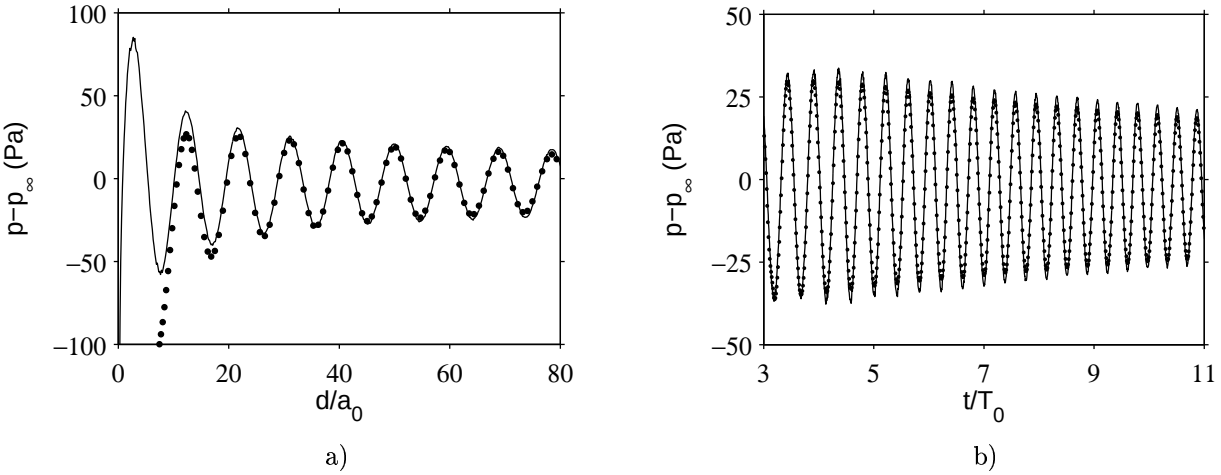

Figure 11. Case $\sigma_0 = 5$. a) Pressure profiles along the line $x = y$, $x > 0$ at time $t = 11T_0$; and b) time history of the pressure at the point $x/a_0 = y/a_0 = 37$: —— analytical solution (4); • computations (d is the distance from the vortex center).

V. Vortices with large aspect ratios $\sigma_0 \geq 6$

In this section, elliptic vortices with large aspect ratios $\sigma_0 \geq 6$ are investigated. For such values, the Kirchhoff elliptic vortex is linearly and nonlinearly unstable for any perturbations. In this case, the growth of instabilities is the dominant process and will cause significant deformations of the vortex. The case $\sigma_0 = 6$ is first considered. The splits of the vortex in the case $\sigma_0 = 25$ is then computed.

For the case $\sigma_0 = 6$, two stages can be distinguished in the time evolution of the vorticity field. In the first stage, an even perturbation grows and splits the ellipse into two co-rotating vortices, as shown by the vorticity snapshots in figure 12. The split is achieved in less than a half revolution. In this case, the growth of instabilities is very rapid and cannot be stopped by the axisymmetrization process. The flow

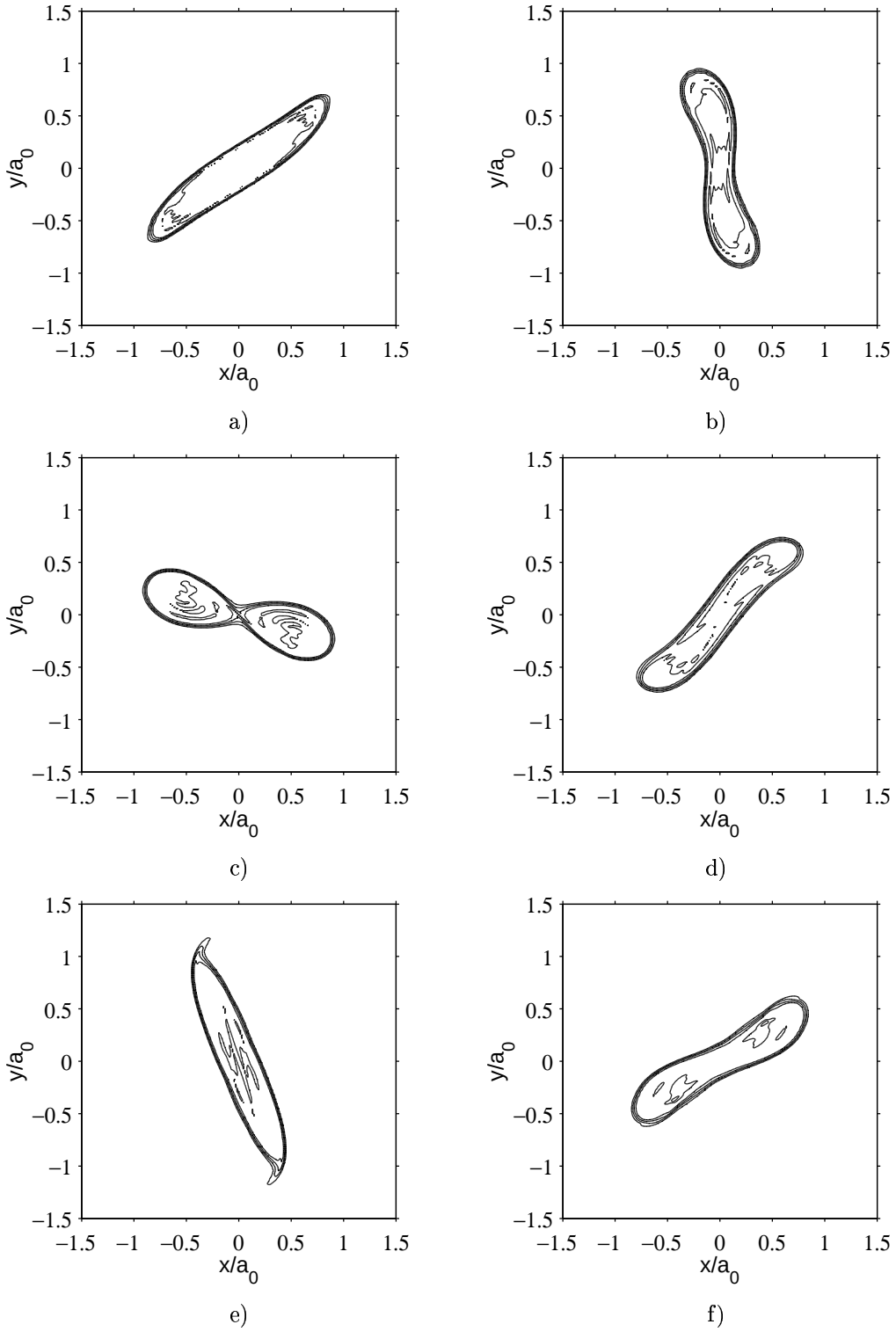

Figure 12. Case $\sigma_0 = 6$. Isolevels of vorticity at successive times. a) $t/T_0 = 0.096$; **b)** $t/T_0 = 0.29$; **c)** $t/T_0 = 0.48$; **d)** $t/T_0 = 0.67$; **e)** $t/T_0 = 0.87$; **f)** $t/T_0 = 1.2$. **Levels: 20%, 40%, 60% and 80% of the maximum of vorticity.**

configuration created by the two vortices is itself unstable. They merge to form a new elliptic vortex with an aspect ratio which remains higher than $\sigma_{4c} \approx 4.61$ as shown in figure 13. Therefore the new vortex is not stable, and a new switch between the two configurations, elliptic vortex and two co-rotating vortices, occurs. Several successive switches are moreover observed. The possibility of such switches has been mentionned by Dritschel,[7,9] who shown, from energetic considerations in the inviscid case, that they may occur more easily for an aspect ratio close to six. Note also that one sequence ellipse/co-rotating vortices/ellipse has been calculated by Vosbeek *et al.*[8] using the contour dynamic method. The time evolution of the aspect ratio σ at each elliptic state is shown in figure 13. The aspect ratio is found to decrease down to 4.8 but it remains larger than σ_{4c}. The initial decrease could be attributed to the filamentation process which is observed in figure 12(e) during the first switch. After three sequences, σ remains around 4.8.

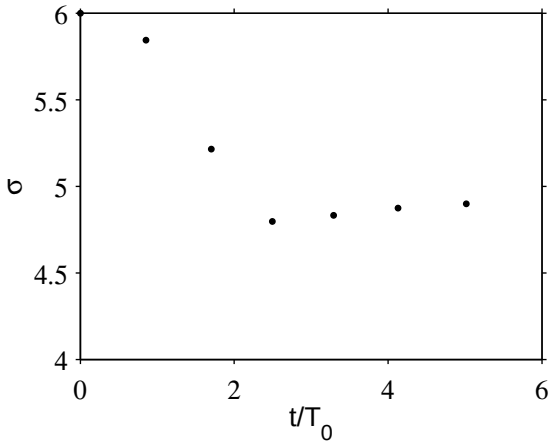

Figure 13. Case $\sigma_0 = 6$. Time history of σ calculated when the vortex has an elliptic shape during the sequences ellipse/co-rotating vortices/ellipse .

The second stage of the vortex evolution begins at time $t \simeq 5.5T_0$. The elliptic vortex definitively splits and a stable configuration with two co-rotating vortices is obtained, as shown by the vorticity field in figure 14. Viscous effects then slowly relaxe gradients making the vortices smoother, see for instance the vorticity snapshots in figures 14(c) and 14(d).

The time history of the pressure at the point $x/a_0 = y/a_0 = 36$ is displayed in figure 15. For $t < 9T_0$, the noise has been generated during the fist aerodynamic stage. Although the vorticity patch is significantly distorted during the switches, the noise remains weakly affected by the successive splits. At about $t = 9T_0$, the radiation level and the frequency suddenly decrease as the final stable configuration is obtained. The sound frequency is then about half of the frequency in the first stage, and the noise level is twice smaller.

One case of very large aspect ratio $\sigma_0 = 25$ is finally computed. Successive vorticity fields of this configuration are reported in figure 16. The initial vortex is very thin and unstable, thus it splits very early, in a quarter of revolution, and generates four aligned vortices, see figure 16(c), as described also by Vosbeek *et al.*[8] Then the two inner vortices merge and three aligned vortices are observed in figure 16(e). Finally, one vortex remains after the merging of these three vortices. Note that in the simulations of Vosbeek *et al.*[8] the evolution of the four aligned vortices is quite different: the two peripheral vortices merge with their closest neighbouring vortex, forming two co-rotating vortices. The reason of this discrepancy is not clear but we can mention that Vosbeek *et al.*[8] used the contour dynamic method and thus do not solve the full Navier–Stokes equations.

The present results show that when the initial aspect ratio is increased, the elliptic vortex splits more rapidly and the number of created vortices is higher. Various mergings can then be obtained before reaching

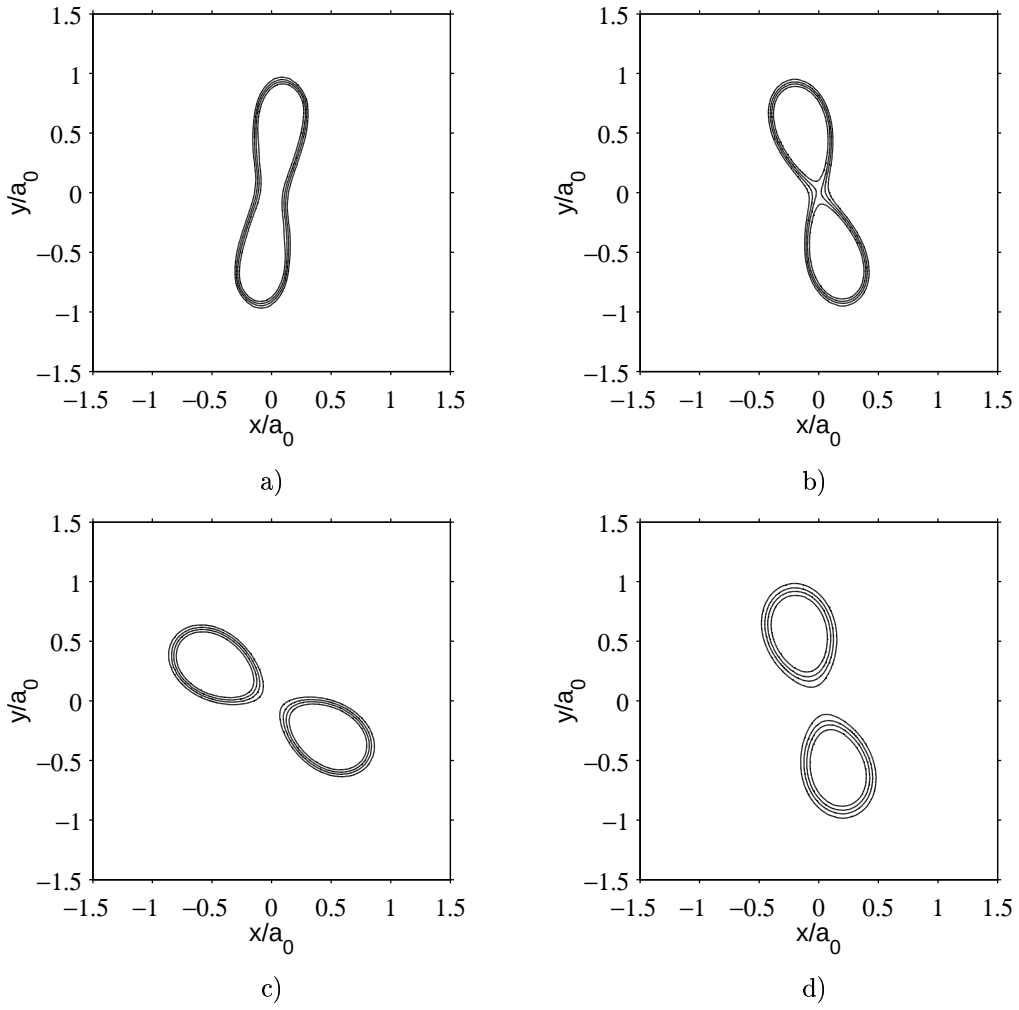

Figure 14. Case $\sigma_0 = 6$. Isolevels of vorticity at successive times. a) $t/T_0 = 2.9$; b) $t/T_0 = 5.8$; c) $t/T_0 = 8.7$; d) $t/T_0 = 19$. Levels: 20%, 40%, 60% and 80% of the maximum of vorticity.

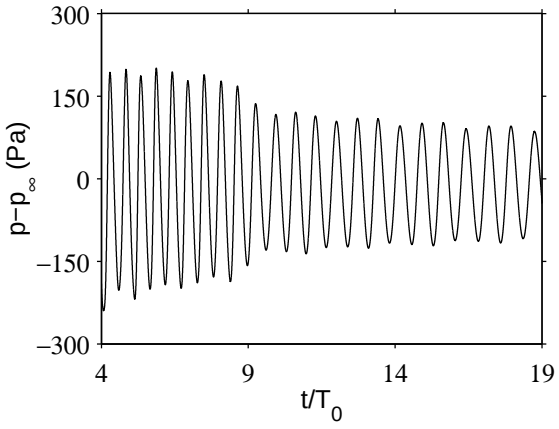

Figure 15. Case $\sigma_0 = 6$. Time history of the pressure at the point $x/a_0 = y/a_0 = 36$.

a stable state with two co-rotating vortices or with an elliptical patch of vorticity. Note that the acoustic field is not investigated in the last case because the aerodynamic evolution of the vortex is too rapid to study properly the acoustic radiation.

VI. Conclusions

In this paper, the aerodynamic behaviours and the acoustic radiations of elliptic vortices with different aspect ratios have been computed. The evolution of the vortex is found to be strongly dependent on the initial aspect ratio. This ratio governs the relative weight of the axisymmetrization process and of the growth of instabilities.

For σ_0 close to unit, neither the filamentation nor the instabilities have a significant effect on the elliptic vortex and on the radiated noise. The vortex rotates with a fixed angular velocity without notable change of shape, and generates a constant and harmonic noise. When σ_0 is larger but remains moderate, about $2 \leq \sigma_0 \leq 6$, the axisymmetrization is the main mechanism and stops the growth of instabilities by stabilizing the vortex. The filamentation occurs and leads to a decrease of the aspect ratio and to an increase of the angular velocity. Then the radiation frequency increases and the noise level decreases. For larger aspect ratios, the growth of instabilities dominates, and the axisymmetrization does not occur rapidly enough to stabilize the vortex. This causes a split of the vortex in several vortices. For $\sigma_0 = 6$, switches between the elliptic state and a state with two co-rotating vortices first happen, before the vortex definitively splits. The sound field remains poorly affected by these switches. Moreover the noise is mainly affected by the decrease of the ellipse aspect ratio and not by the presence of the filaments. The ellipse parameter ϵ is therefore the key parameter to describe the acoustic radiation of the elliptic vortex. Finally, the computed sound field is shown to be in good agreement with the analytical formulation of the radiated noise exposed in the appendix.

The validity of the present computational approach is clearly shown. The computations have been performed by Direct Numerical Simulation and the acoustic radiation is obtained in the same calculation. This enables to take into account all effects, in particular compressibility and viscous diffusion. Such an approach can be used to investigate the aerodynamic behaviours and the acoustic radiations of more sophisticated two-dimensional and three-dimensional flows.

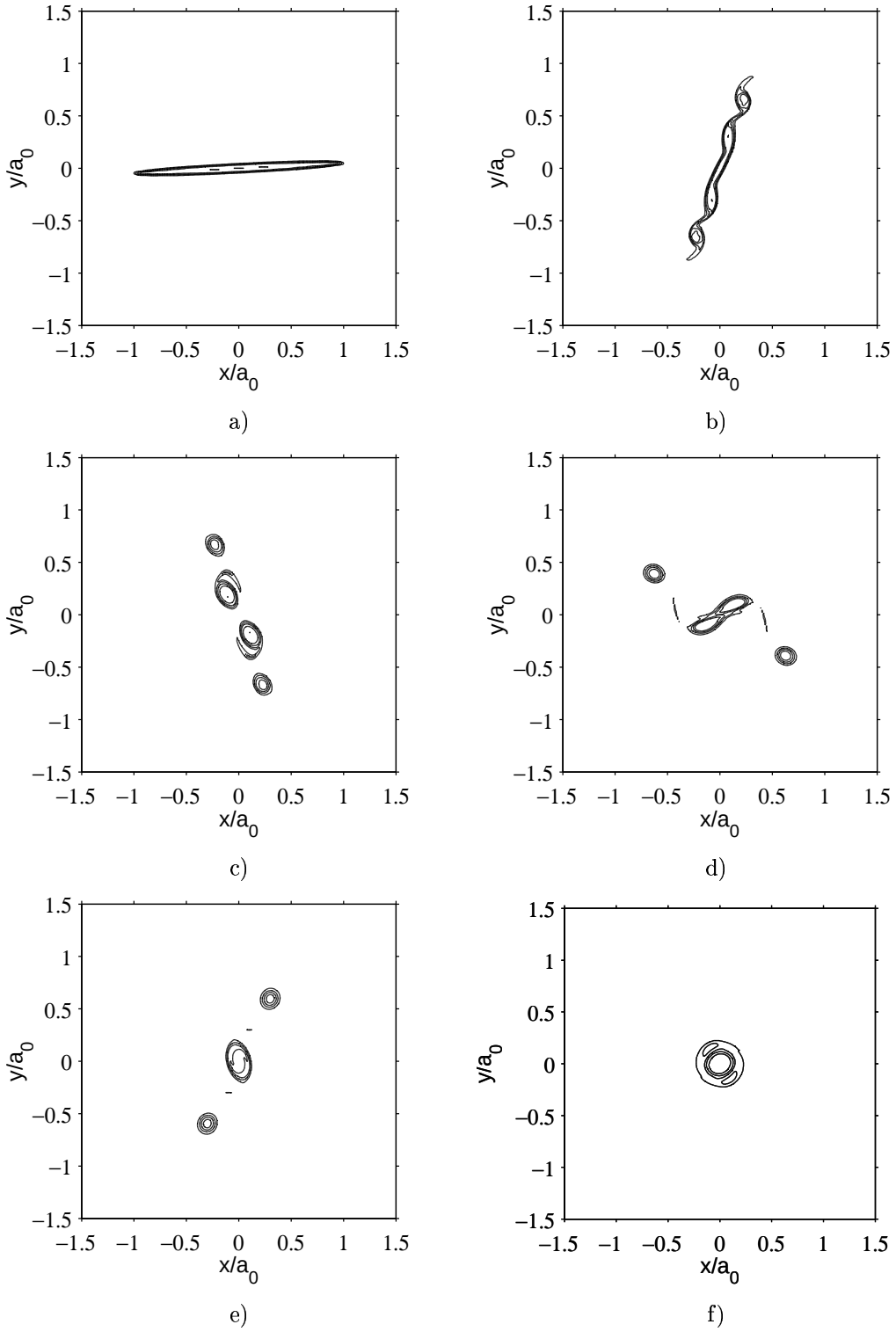

Figure 16. Case $\sigma_0 = 25$. Isolevels of vorticity at successive times. a) $t/T_0 = 8.1 \times 10^{-3}$; b) $t/T_0 = 0.20$; c) $t/T_0 = 0.32$; d) $t/T_0 = 0.46$; e) $t/T_0 = 0.81$; f) $t/T_0 = 1.13$. Levels: 20%, 40%, 60% and 80% of the maximum of vorticity.

Appendix: analytical formulation of the noise radiated by the Kirchhoff vortex

In this appendix, an analytical formulation of the far-field noise radiated by the Kirchhoff vortex is reported. The way used to derive the solution has been presented by Howe[19] and Crighton *et al.*[21] The viscous effects and the fluctuations of entropy are neglected. An incompressible flow bounded by a volume V is considered. The velocity and the vorticity of the flow field are noted respectively $\boldsymbol{u}$ and $\boldsymbol{\omega}$. According to the Powell analogy, the fluctuations of ρ outside the flow can be expressed by:

$$\rho'(t,\boldsymbol{x}) \approx \frac{\rho_\infty}{4\pi c_\infty^2}\frac{\partial}{\partial x_i}\int_V (\boldsymbol{\omega}\wedge\boldsymbol{u})_i \left(\boldsymbol{y}, t-\frac{|\boldsymbol{x}-\boldsymbol{y}|}{c_\infty}\right)\frac{\mathrm{d}\boldsymbol{y}}{|\boldsymbol{x}-\boldsymbol{y}|} \tag{1}$$

where ρ_∞ and c_∞ are respectively the mean density and the mean sound velocity in the ambient medium. By considering only the far-field noise, this expression becomes:

$$\rho'(t,\boldsymbol{x}) \approx -\frac{\rho_\infty}{4\pi c_\infty^4|\boldsymbol{x}|}\frac{x_i x_j}{|\boldsymbol{x}|^2}\frac{\partial^2}{\partial t^2}\int_V y_j\,(\boldsymbol{\omega}\wedge\boldsymbol{u})_i \left(\boldsymbol{y}, t-\frac{|\boldsymbol{x}|}{c_\infty}\right)\mathrm{d}\boldsymbol{y} \tag{2}$$

This formulation is now applied to the Kirchhoff elliptic vortex. The velocity distribution within the vortex is given, in polar coordinates, by:

$$\boldsymbol{u} = -\frac{\omega r}{2}\left|\begin{array}{l}\sin(\theta)+\epsilon\sin\left(\theta-\frac{1-\epsilon^2}{2}\omega t\right)\\ -\cos(\theta)+\epsilon\cos\left(\theta-\frac{1-\epsilon^2}{2}\omega t\right)\end{array}\right.$$

These expressions are valid for any values of ϵ. In what follows, it is assumed that $\epsilon \ll 1$. Thus only the first order in ϵ is kept. Within this restriction, the shape of the vortex in polar coordinates is $r = r_e[1+\epsilon\cos(2\theta-\omega t/2)]$ and the angular velocity becomes $\Omega_1 = \omega/4$. By using the method of the stationnary phase and the relation $p(t,r,\theta)-\overline{p}(r,\theta) \approx c_\infty^2\rho'(t,r,\theta)$, the pressure field can be written as:

$$p(t,r,\theta)-\overline{p}(r,\theta) \approx -\frac{\epsilon}{8}\left(\frac{2\pi r_e}{r}\right)^{1/2}\rho_\infty U^2 M^{3/2}\cos\left(2\theta-\frac{\omega t_r}{2}+\frac{\pi}{4}\right) \tag{3}$$

with $U = r_e\omega/2$, $M = U/c_\infty$ and t_r is the retarded time $t - r/c_\infty$. This expression applies only to the far-field of a Kirchhoff elliptic vortex with an aspect ratio σ close to unit. The acoustic field decreases like $r^{-1/2}$, as expected for the far-field in a two-dimensional problem. Note that the amplitude is proportional to the ellipse parameter ϵ, whereas the frequency of the noise is constant and does not depend on ϵ. Thus, the effect of ϵ on the frequency is not taken into account in this expression.

As shown in the present paper, vortices with an initial aspect ratio not close to unit do not keep a uniform shape. The aspect ratio and the angular velocity evolve with time. In such cases, the quantities in the expression (3) have to be considered at the retarded time t_r, to take into account the propagation time between the generation and the reception of the noise. Moreover, when the aspect ratio is not close to unit, the approximated angular velocity $\Omega_1 = \omega/4$ might significantly differ from the theoretical angular velocity $\Omega_{th} = \omega(1-\epsilon^2)/4$ and, consequently, from the effective velocity. In this case, the expression (3) might fail in providing the radiation frequency. An extended formulation, which includes the influence of ϵ in both the amplitude and the frequency, can then be obtained by observing that $\omega t_r/4$ is the angular position of the vortex, α_r, at the retarded time t_r. In the case of an elliptical vortex with an aspect ratio and an angular velocity evolving with time:

$$p(t,r,\theta)-\overline{p}(r,\theta) \approx -\frac{\epsilon_r}{8}\left(\frac{2\pi r_{er}}{r}\right)^{1/2}\rho_\infty U_r^2 M_r^{3/2}\cos\left(2(\theta-\alpha_r)+\frac{\pi}{4}\right) \tag{4}$$

where the subscript r denotes a quantity taken at the retarded time t_r. This new expression is expected to provide a better description of the radiation frequency than expression (3), because the frequency is directly linked to the effective motion of the vortex.

Acknowledgments

The first author is grateful to the Centre National d'Études Spatiales (CNES) for financial support.

References

[1]Miyazaki, T. and Hanazaki, H., "Baroclinic Instability of Kirchhoff's Elliptic Vortex," *J. Fluid Mech.*, Vol. 261, 1994, pp. 253–271.

[2]Miyazaki, T., Hirahara, K., and Hanazaki, H., "The Quasi-Three-Dimensional Instability of an Elliptical Vortex Subject to a Strain Field in a Rotating Stratified Fluid," *Fluid Dyn. Research*, Vol. 21, 1997, pp. 359—380.

[3]Dritschel, D. G. and Legras, B., "The Elliptical Model of Two-Dimensional Vortex Dynamics. II: Disturbance Equations," *Phys. Fluids*, Vol. 3, No. 5, 1991, pp. 855–869.

[4]Legras, B. and Dritschel, D. G., "The Elliptical Model of Two-Dimensional Vortex Dynamics. I: The Basic State," *Phys. Fluids*, Vol. 3, No. 5, 1991, pp. 845–854.

[5]Lamb, H., *Hydrodynamics*, Dover, 6th ed., 1932.

[6]Love, A. E. H., "On the Stability of Certain Vortex Motions," *Proc. Lond. Math. Soc.*, Vol. 35, 1893, pp. 18–42.

[7]Dritschel, D. G., "The Nonlinear Evolution of Rotating Configurations of Uniform Vorticity," *J. Fluid Mech.*, Vol. 172, 1986, pp. 157–182.

[8]Vosbeek, P. W. C., van Heijst, G. J. F., and Mogendorff, V. P., "The Strain Rate in Evolution of (Elliptical) Vortices in Inviscid Two-Dimensional Flows," *Phys. Fluids*, Vol. 13, No. 12, 2001, pp. 3699–3708.

[9]Dritschel, D. G., "The Stability and Energetics of Corotating Uniform Vortices," *J. Fluid Mech.*, Vol. 157, 1985, pp. 95–134.

[10]Melander, M. V., McWilliams, J. C., and Zabusky, N. J., "Axisymmetrization and Vorticity-Gradient Intensification of an Isolated Two-Dimensional Vortex Through Filamentation," *J. Fluid Mech.*, Vol. 178, 1987, pp. 137–159.

[11]Melander, M. V., Zabusky, N. J., and McWilliams, J. C., "Symmetric Vortex Merger in Two Dimensions: Causes and Conditions," *J. Fluid Mech.*, Vol. 195, 1988, pp. 303–340.

[12]Dritschel, D. G., "On the Persistence of Non-Axisymmetric Vortices in Inviscid Two-Dimensional Flows," *J. Fluid Mech.*, Vol. 371, 1998, pp. 141–155.

[13]Bogey, C. and Bailly, C., "A Family of Low Dispersive and Low Dissipative Explicit Schemes for Noise Computation," *J. Comp. Phys.*, Vol. 194, No. 1, 2004, pp. 194–214.

[14]Bogey, C., Bailly, C., and Juvé, D., "Noise Investigation of a High Subsonic, Moderate Reynolds Number Jet Using a Compressible LES," *Theoret. Comput. Fluid Dynamics*, Vol. 16, No. 4, 2003, pp. 273–297.

[15]Bogey, C. and Bailly, C., "Investigation of Subsonic Jet Noise Using LES: Mach and Reynolds Number Effects," *10th AIAA/CEAS Aeroacoustics Conference 10-12 may, Manchester, UK*, 2004, pp. 2004–3023.

[16]Gloerfelt, X., Bailly, C., and Juvé, D., "Direct Computation of the Noise Radiated by a Subsonic Cavity Flow and Application of Integral Methods," *J. Sound Vib.*, Vol. 266, No. 1, 2003, pp. 119–146.

[17]Colonius, T., Lele, S. K., and Moin, P., "Sound Generation in a Mixing Layer," *J. Fluid Mech.*, Vol. 330, 1997, pp. 375–409.

[18]Bogey, C., Bailly, C., and Juvé, D., "Numerical Simulation of the Sound Generated by Vortex Pairing in a Mixing Layer," *AIAA Journal*, Vol. 38, No. 12, 2000, pp. 2210–2218.

[19]Howe, M. S., "Contributions to the Theory of Aerodynamic Sound, With Application to Excess Jet Noise and the Theory of the Flute," *J. Fluid Mech.*, Vol. 71, 1975, pp. 625–673.

[20]Tam, C. K. W. and Webb, J. C., "Dispersion-Relation-Preserving Finite Difference Schemes for Computational Acoustics," *J. Comp. Phys.*, Vol. 107, 1993, pp. 262–281.

[21]Crighton, D. G., Dowling, A. P., Williams, J. E. F., Heckl, M., and Leppington, F. G., *Modern Methods in Analytical Acoustics*, Springer, 1992.